Influence of stress triaxiality and strain rate on stress-strain behaviour and dilation of mineral-filled PVC

Sindre Olufsen*, Arild Holm Clausen, Odd Sture Hopperstad

Structural Impact Laboratory (SIMLab), Department of Structural Engineering, NTNU, Norwegian University of Science and Technology, NO-7491 Trondheim, Norway

**Corresponding author: Email address: sindre.n.olufsen@ntnu.no (Sindre Olufsen)*

Abstract

The influence of stress triaxiality and strain rate on the tensile behaviour of mineral-filled polyvinyl chloride (PVC) is investigated in this paper. Axisymmetric notched tensile specimens with notch radius equal to 20 mm, 5 mm and 2 mm were tested at three nominal strain rates of 0.0001/s, 0.001/s and 0.01/s. Surface deformations were measured by digital image correlation and contour tracking, employing two orthogonal cameras, whereas infrared thermography was used to measure self-heating. The yield strength of the material was found to be strain rate and pressure dependent. The volume change was estimated from the stretch field in the notch region of the specimens and found to depend on both stress triaxiality and strain rate. A marked increase of temperature was measured at the highest strain rate.

Keywords: Tensile tests, Notched specimens, Digital image correlation, Contour tracking, Infrared thermography

1 Introduction

Polymeric materials are nowadays the most common group of materials used in consumer products, largely due to their low price, a wide range of favourable properties and good manufacturability. The quantities of polymeric materials produced globally and the typically slow biodegradability of polymers impose challenges with regards to recycling, and motivate improved mechanical design to reduce material usage. The mechanical design of components made of polymeric materials with regards to structural integrity is a challenge, as the influence of viscosity, ageing, anisotropy and production parameters must be accounted for. The finite element method (FEM) has become the dominant tool in the design process, and the numerical model must incorporate the relevant characteristics for the behaviour of the polymer to be used. Key ingredients in a material model are a constitutive relation, which describes the stress as function of strain, strain rate and temperature, and a failure criterion. Considering amorphous polymers, the failure behaviour spans from brittle failure in un-toughened polycarbonate [1] to ductile failure in PVC [2]. The factors influencing a polymer's ability to sustain large plastic strains have been investigated since the early days of thermoplastic materials, and important features include microstructure, inclusions, loading rate and stress triaxiality.

Void nucleation and growth, either in the localized form of crazing [3–6] or as distributed voids [7–10], have been established as the damage mechanisms governing ductile failure of many amorphous polymers. As can been seen in experimental studies, e.g. by Boisot et al. [7], Brusselle-Dupend et al. [8] and G'Sell et al. [5], damage evolution occurs in the form of volume dilation on the macro-scale and the formation and growth of voids on the micro-scale. The rate of void growth is observed to depend on stress triaxiality [2,7]. Micro-voiding in polymers has also been the subject of numerical studies, see for instance Steenbrink et al. [11], Chew et al. [12] and Cheng and Guo [13].

The correlation between the presence of micro-structural inhomogeneities or inclusions and the tendency of a material to form voids during deformation has, among others, been reported by Ognedal et al. [2]. Filler materials in the form of small particles are commonly used additives in amorphous polymers to improve the mechanical properties [14] and, in some cases, to reduce the costs. For amorphous polymers containing filler particles, cavitation within the particle or de-cohesion of the particle-matrix interface followed by void growth has been investigated [2,11]. The particle adhesion and filler particle size have been found to have an influence on the toughness and strength of the resulting polymer nano-composite, see Fu et al. [14].

Strain softening at the onset of yielding is a phenomenon often observed during large-scale deformation of an amorphous polymer, and has been attributed to different mechanisms such as ageing [15], void nucleation and void growth [11,16]. Strain softening along with low subsequent strain hardening promotes strain localization at the onset of yielding, and represents a challenge with respect to strain acquisition. The current state-of-the-art in digital image correlation (DIC) allows for local strains to be acquired even during strain localization [17], and the volume distribution of voids within a deformed specimen can be obtained by methods such as X-ray tomography [6,18,19].

Surface deformations have long been used for the estimation of volumetric changes within tensile specimens, based on assumptions regarding the internal deformation of the specimen. Laiarinandrasana et al. [10] demonstrated by means of X-ray tomography that the radial distribution of voids in a PA6 material was both complex and non-stationary, thus questioning the accuracy of volumetric strain estimates based on surface measurements. Consequently, surface measurements can only provide an average quantification of the change of volume. On the other hand, an accurate description of the contour of the specimen may be useful for comparison with finite element simulations incorporating dilation. Validation of such material models calls for experimental tests where both local and global response parameters can be compared with the numerical predictions.

In order to design an experiment where the influence of stress triaxiality can be investigated, it is required that at least the initial stress state within the specimen is well defined. This can be obtained by applying notched tensile specimens, frequently used due to their ease of manufacturing, axis-symmetry and analytically defined stress state [2,18–20]. Due to the complex geometry, full field techniques, such as DIC, are necessary for accurate strain measurements, even at small strains.

Building on previous studies [2,16,17,21], this article investigates the influence of strain rate and stress triaxiality on the stress-strain behaviour and dilation of a mineral-filled PVC during monotonic tensile loading using global FEM-based DIC software, specimen contour tracing and thermal imaging. In order to obtain a triaxial stress state with a predefined initial stress triaxiality ratio, axisymmetric notched tensile specimens were employed. The use of the triaxiality ratios investigated was motivated by their relevance for industrial applications as well as ease of manufacturing and instrumentation. Compared to the previous studies, the possibility to measure the deformation of a single material point, even at large strains, gives new insight into the material's plastic response, being of particular interest for the development of constitutive models. The average true stress in the minimum cross-section is chosen as the appropriate stress measure, using a continuously updated cross-sectional area. Combined with the logarithmic strain in the longitudinal direction of the specimen extracted from the notch root, the material's tensile response was measured beyond the point of necking. Contour tracking gives additional information of the strain localization within the notch region, as the surface curvature can be linked to the internal stress field of the specimen, as well as providing verification of constitutive models. Plastic dilation due to void formation and growth is here estimated based on local measures, providing an experimental basis for verification of damage models. Due to the inherent uncertainties related to the methodology used for estimating plastic dilation, the results are considered qualitative, but still provide valuable information of damage evolution. In the following, Section 2 outlines the experimental set-up, data acquisition protocol, and the subsequent calculation of relevant response parameters. The results from the tension tests at three levels of strain rate on samples with three different initial notch radii follow in Section 3. A discussion of the results is provided in Section 4, before the main conclusions are drawn in Section 5.

2 Materials and methods

2.1 Materials

A mineral-filled PVC with an estimated $CaCO_3$ particle content of approx. 40 weight % was investigated. The particle content was determined by means of thermogravimetric analysis and the corresponding volume fraction was approx. 25%. The material was extracted from 10 mm thick extruded plates provided by Kömmerling.

The material was inspected using scanning electron microscopy (SEM) employing a Hitachi S3400 microscope with an accelerator voltage of 10 kV. Liquid nitrogen was used to cool small material specimens such that brittle fracture was initiated when the specimen was split. Gold coating was applied to the fracture surface prior to the SEM investigation. A micrograph acquired of such a fracture surface is shown in Figure 1. From the micrographs, two groups of particles are uncovered, being small spherical particles with typical diameter in the range of 0.2-0.4 μm and larger irregular particles. The particles appear to be well dispersed. EDS was used to investigate the composition of the particles, confirming that both groups of particles consist of CaCO3. These findings agree with previous investigations on a similar material by Ognedal et al. [16].

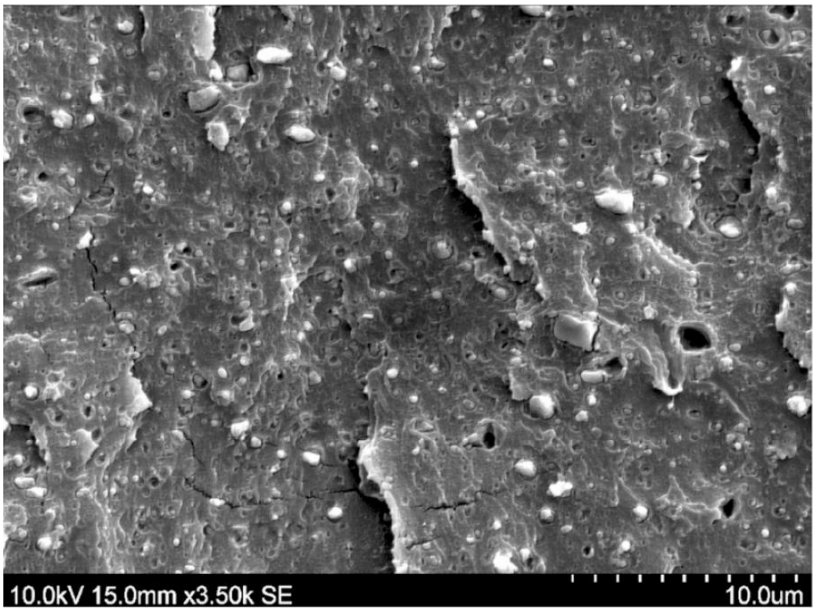

Figure 1 Micrograph from fracture surface of a PVC sample showing CaCO3 particles embedded in a PVC matrix.

2.2 Test specimens

Axisymmetric notched tensile specimens were employed, allowing the initial stress triaxiality in the notch section of the specimen to be varied. In the tests, specimens with notch radii of 20 mm, 5 mm and 2 mm were used, hereafter referred to as R20, R5 and R2 specimens, respectively. According to the Bridgman formula, the three notch radii correspond to an initial stress triaxiality of approx. 0.4, 0.6 and 0.8, respectively, at the centre of the minimum cross section. The use of this range was motivated by its relevance for engineering applications as well as practical considerations during the preparation of the specimens. The geometry of the three specimens is shown in Figure 2.

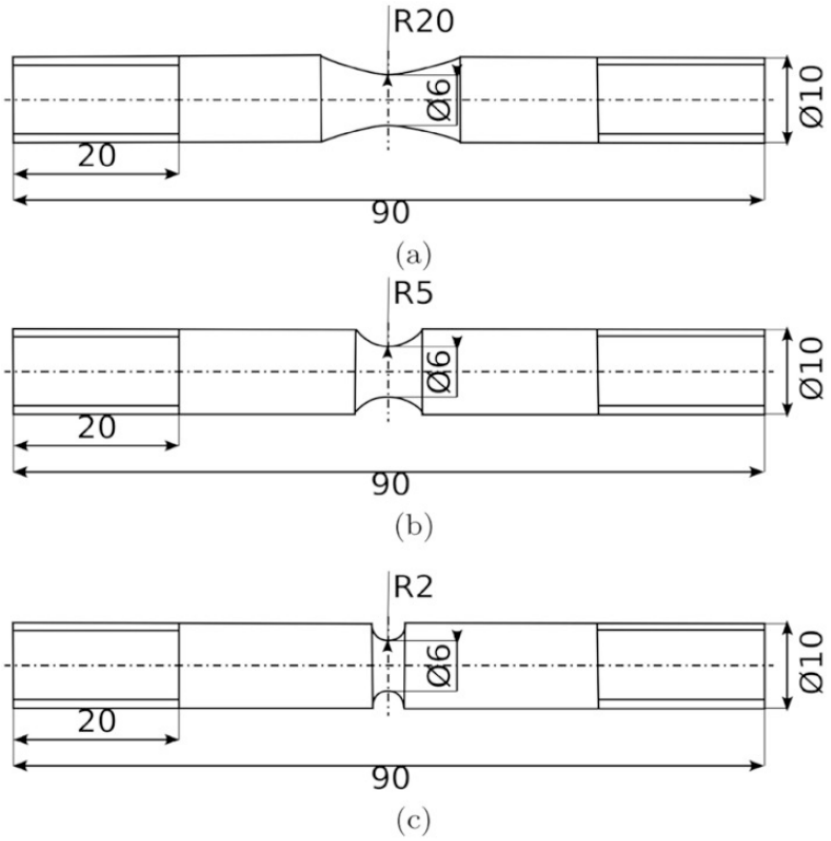

Figure 2 Specimens with notch radius (a) R = 20 mm, (b) R = 5 mm and (c) R = 2 mm. Measures in mm.

The notched tensile specimens were manufactured from the 10 mm thick extruded plates employing a lathe, and care was taken to avoid bending and excessive heating during the turning process. The minimum diameter of all specimens was measured manually before each test. The longitudinal axis of the specimens was oriented coaxially with the extrusion direction of the plates, and the out-of-plane direction of the plate was marked on each specimen. Fixing the specimen in the tensile test machine was obtained by threading of the specimens at both ends.

To facilitate digital image correlation, a speckle pattern was applied to all specimens using an airbrush. Further, the part of the specimen facing the thermal camera was painted black to ensure emissivity of infrared light corresponding to the calibration of the camera.

2.3 Experimental set-up

Tensile testing was performed employing an Instron 5082 tensile test machine with a 2 kN load cell, synchronized with the two digital cameras. The experimental set-up is shown in Figure 3. Digital image correlation was facilitated by two Proscilica GC2450 cameras equipped with a 105 mm Nikon lens and a 105 mm Sigma lens, both monitoring the notch section. One of the cameras was aligned with the out-of-plane direction of the plate from which the specimen was machined and the other was orthogonal to this direction and to the longitudinal axis of the specimen. A sufficient focus depth in the entire region of interest was ensured by applying an aperture of F12.0

for both cameras. To simplify the extraction of the specimen contour from the images, increased contrast between the specimen and the background was obtained by additional lighting of the background. The surface temperature was measured using a FLIR SC 7500 thermal camera aimed at the rear part of the specimen, see Figure 3.

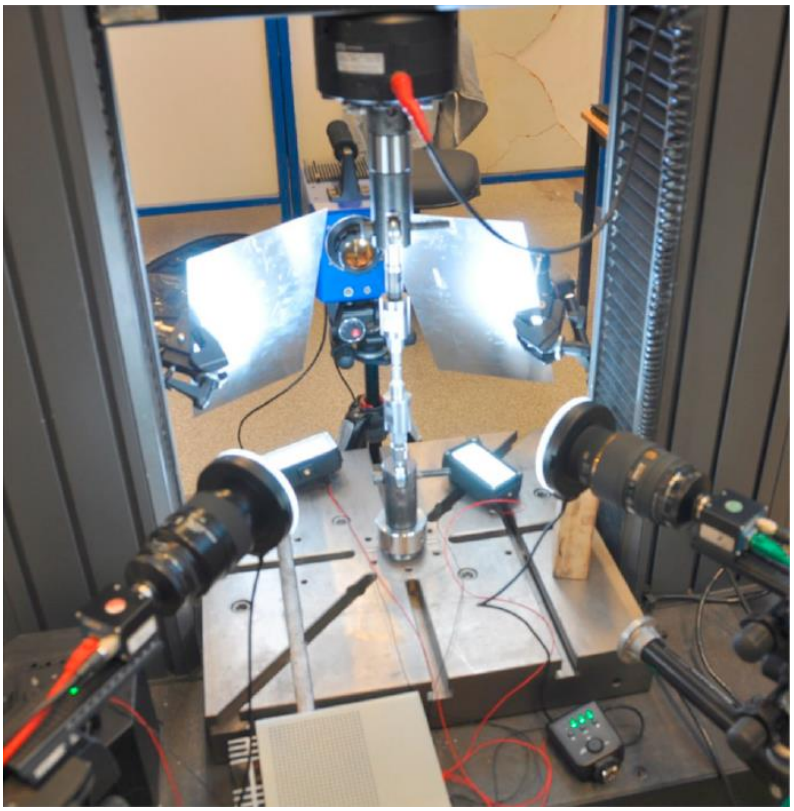

Figure 3 Experimental set-up showing two cameras with ring-lighting, the thermal camera and two reflectors with lighting.

Three target nominal strain rates of 10^{-4} s^{-1}, 10^{-3} s^{-1} and 10^{-2} s^{-1} were applied in the tests. This range was chosen to avoid excessive self-heating during deformation, yet having relevance for several engineering applications. In order to get an indication of the repeatability of the experiments, two or three repeat tests were carried out for each combination of nominal strain rate and notch radius. All specimens were elongated until rupture.

As there is no defined gauge length, a constant cross-head velocity corresponding to the chosen initial strain rates of 10^{-4} s^{-1}, 10^{-3} $s^{-1}$and 10^{-2} s^{-1} was determined by running virtual experiments with a finite element code using a previously calibrated material model [17]. Targeting a nominal strain rate of 10^{-4} s^{-1}, cross-head velocities of 2.8×10^{-3}mm/s, 3.2×10^{-3}mm/s and 3.7×10^{-3} mm/s were used for the R2, R5 and R20 specimens, respectively. To obtain the nominal strain rates of 10^{-3} s^{-1} and 10^{-2} s^{-1}, the crosshead velocity was increased by a factor of 10 and 100, respectively. The camera frame rate was chosen such that about 550 frames were captured during the test for the nominal strain rates of 10^{-4} s^{-1} and 10^{-3} s^{-1}. In the tests with a nominal strain rate of 10^{-2} s^{-1}, limited light intensity, and hence a lower bound in shutter time, yielded 150 frames during the test.

2.4 Measurement of notch root curvature

A circle was fitted to the notch root by means of a non-linear least squares method using the centre position and the circle radius as optimization variables. The width of the notch root segment to which the circle was fitted was chosen such that it was smaller than a potential neck induced by strain localization. As the shoulders of the neck region were diffuse for some specimens, they were found manually from the last frames in each image series.

2.5 Measurement of strain and stress

The deformation field at the surface of the specimen was measured by means of two-dimensional (2D) digital image correlation using an in-house code. The global DIC code employs Q16 finite elements having bi-cubic shape functions, and these elements have been shown to perform well for large strain analysis of polymer materials [17].

Within the notch, the section with the largest longitudinal strain was identified, and mesh convergence in this region of interest was ensured by reducing the element size until no further change in longitudinal strain was obtained. To avoid interpolation of the deformation gradient across element boundaries, the region of interest was centred within one element row which, due to the use of higher order elements, can represent a parabolic strain field. As only projected deformations were captured on the curved surface of the axisymmetric samples, only the deformation gradient along the circumference of the notch root was used.

The longitudinal, circumferential and radial stretch ratios, denoted respectively λ_l, λ_c and λ_r, were determined from the deformation gradient extracted along the circumference of the specimen notch. The average longitudinal stretch ratio is the average of the longitudinal stretch along the visible circumference of the specimen. The average radial stretch component is not directly available from the 2D DIC analysis and is, therefore, approximated as:

$$\lambda_r = \frac{D}{D_0} = \frac{\Sigma_{i=1}^{n} \Delta D_i}{\Sigma_{i=1}^{n} \Delta D_{0,i}} = \frac{\Sigma_{i=1}^{n} \lambda_{r,i} \Delta D_{0,i}}{\Sigma_{i=1}^{n} \Delta D_{0,i}} = \frac{\Sigma_{i=1}^{n} \lambda_{r,i}}{n} \quad (1)$$

where D and D_0 are, respectively, the current and initial specimen diameters, ΔD_i and $\Delta D_{0,i}$ are the current and initial diameter segments, $\lambda_{r,i}$ is the corresponding radial stretch mapping $\Delta D_{0,i}$ to ΔD_i as $\Delta D_i = \lambda_{r,i} \Delta D_{0,i}$, and n is the number of segments along the visible circumference. As the pixels have uniform size, the segment length $\Delta D_{0,i}$ is here set to an arbitrary finite value, being equal for all segments i. The circumferential stretch λ_c is equal to $\lambda_{r,c}$, where the index $i = c$ corresponds to the segment located at the centre of the notch root, ensuring that the stretch direction is orthogonal to the camera axis.

The logarithmic strain components ε_j were then determined from the corresponding stretch ratios as:

$$\varepsilon_j = \ln(\lambda_j) \quad (2)$$

where j denotes the components l, c and r, referring respectively to the longitudinal, circumferential and radial directions. Henceforth, the logarithmic strain ε_l in the longitudinal direction of the specimen will simply be denoted as the true strain.

The average true stress σ in the section of minimum diameter within the notch region of the specimen was calculated as:

$$\sigma = \frac{4F}{\pi D^2} \tag{3}$$

where F is the force measured by the load cell and D is the smallest diameter in the notch region, as continuously evaluated during the test by digital image correlation.

The average volume ratio λ_V, defined as the ratio between the current volume V and the initial volume V_0 of an infinitesimally thin disc through the minimum diameter of the notch region of the specimen, can be estimated based on the external geometry of the specimen during deformation as:

$$\lambda_V = \frac{V}{V_0} = \lambda_l \lambda_r^2 \tag{4}$$

Since λ_V is entirely based on surface measurements, it should be considered to provide qualitative information of the volume change within the measured region.

2.6 Measurement of surface temperature

From the thermographic images, the surface temperature in the root of the notch was determined as the average temperature along the visible circumference at the section with minimum diameter. The ambient temperature in the laboratory, and hence the initial surface temperature of the specimens, was 24°C.

3 Results

Addressing a representative sample of each type of initial notch radius, Figure 4 shows pictures of the deformed specimens just before visible surface cracking was observed. The nominal strain rate was 10^{-4} s^{-1} in all these tests. The corresponding true strain field is also included in Figure 4, and it appears that strains of the order of unity occur in the notch region of the specimens. The largest strains were found in the R2 specimens.

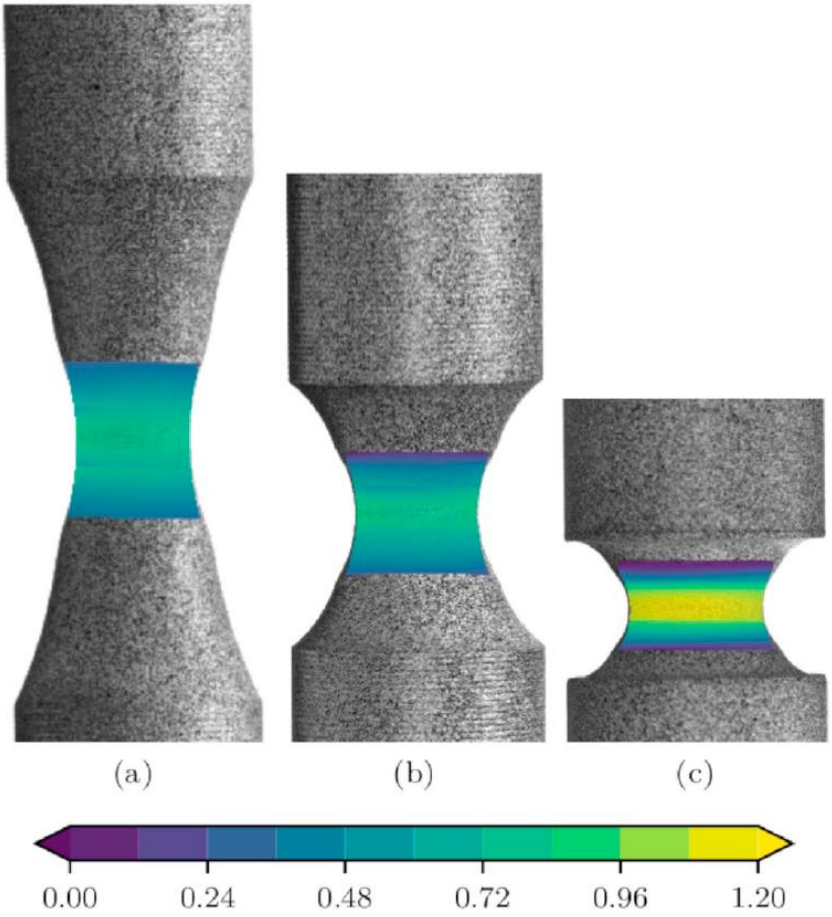

Figure 4 Deformed state and true strain field for specimen with notch radius (a) R = 20 mm, (b) R = 5 mm and (c) R = 2 mm at strain rate of 10^{-4} s^{-1}.

Figure 5 shows the true stress vs. true strain curves for all tests, where the true strain and the true stress were determined from Equation 2 and Equation 3, respectively. The sub-figures address the specimens with three different notch radii, see Figure 2. All curves are plotted up to the onset of failure. The initial stress-strain response before strain softening is similar for all specimens. Strain softening occurs at higher stress levels for higher strain rates, but is only marginally affected by the initial notch radius. The strain softening is followed by strain hardening in all the tensile tests, except for the R2 specimens at a strain rate of 10^{-2} s^{-1}. The stress drop during the softening stage depends on the specimen geometry and, to some extent, the strain rate. It is most pronounced for the R5 and R20 specimens and the highest strain rate. Further, Figure 5 shows that the scatter between replicate tests is limited, in particular for the stress-strain response up to failure. The failure strain, however, differs slightly among the parallel tests.

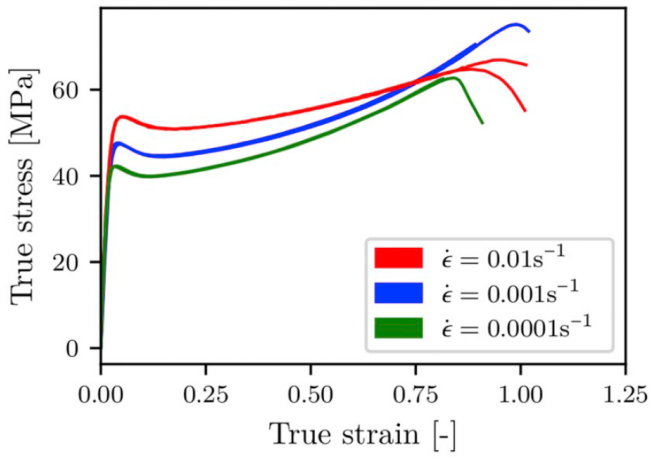
True stress [MPa]
0
20
40
60
0.00
0.25
0.50
0.75
1.00
1.25
True strain [-]
$\dot{\epsilon} = 0.01\text{s}^{-1}$
$\dot{\epsilon} = 0.001\text{s}^{-1}$
$\dot{\epsilon} = 0.0001\text{s}^{-1}$

(a)

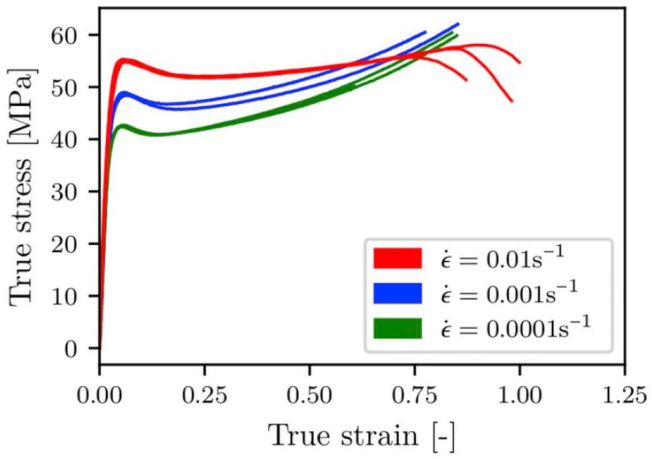
True stress [MPa]
0
10
20
30
40
50
60
0.00
0.25
0.50
0.75
1.00
1.25
True strain [-]
$\dot{\epsilon} = 0.01\text{s}^{-1}$
$\dot{\epsilon} = 0.001\text{s}^{-1}$
$\dot{\epsilon} = 0.0001\text{s}^{-1}$

(b)

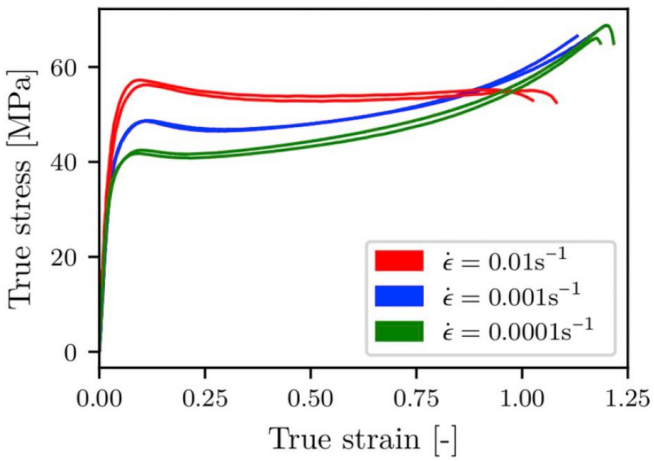
True stress [MPa]
0
20
40
60
0.00
0.25
0.50
0.75
1.00
1.25
True strain [-]
$\dot{\epsilon} = 0.01\text{s}^{-1}$
$\dot{\epsilon} = 0.001\text{s}^{-1}$
$\dot{\epsilon} = 0.0001\text{s}^{-1}$

(c)

Figure 5 True stress vs. true strain curves for specimens with notch radius (a) R = 20 mm, (b) R = 5 mm and (c) R = 2 mm at three levels of strain rate.

The yield stress is defined as the stress at the local stress maximum where softening is initiated, and is presented as function of nominal strain rate in Figure 6 for all specimens. A log-linear increase of the yield stress with increasing strain rate is observed. The yield stress is almost independent of notch radius for strain rates 10^{-4} s^{-1} and 10^{-3} s^{-1}, whereas a small increase of the yield stress with decreasing notch radius is observed for a strain rate of 10^{-2} s^{-1}.

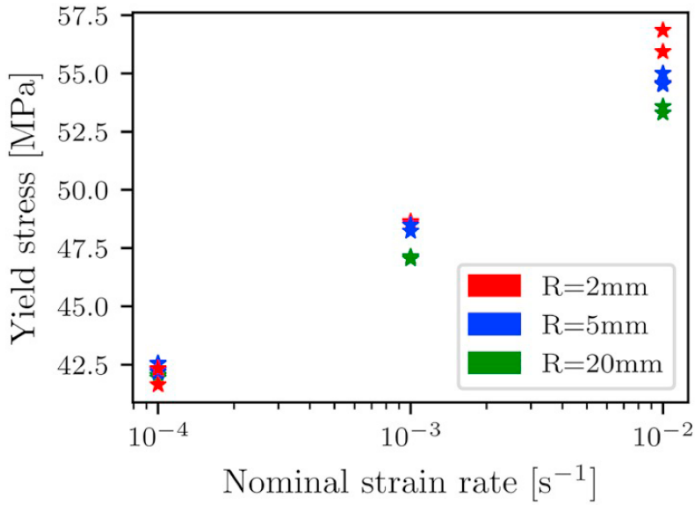

Figure 6 Yield stress vs. nominal strain rate for the notched specimens.

The average true strain rate at the minimum diameter of the notch is shown as a function of true strain in Figure 7 for all specimens. The sub-figures address the three different nominal strain rates. To obtain the local true strain rate, a Savitzky-Golay filter [22] was first applied to the true strain vs. time curve, and thereafter the true strain data were differentiated numerically with respect to time. The filter window was chosen such that the shape of the strain rate curve was preserved, but still suppressing high frequency noise. Figure 7 demonstrates that the local true strain rates are an order of magnitude higher than the nominal strain rates during the experiments. A peak in local true strain rate is observed for all nominal strain rates after the onset of yielding and thereafter it decreases steadily with strain. The peak is most pronounced for nominal strain rates 10^{-4} s^{-1} and 10^{-3} s^{-1}, while for a nominal strain rate of 10^{-2} s^{-1}, the local true strain rate maintains an approximately constant value until failure for the R20 and R5 specimens. A local increase of the strain rate immediately before failure is also observed in most tests.

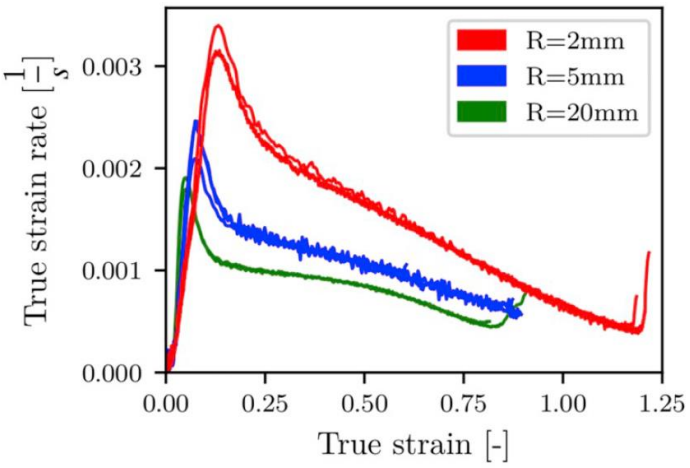
R=2mm
R=5mm
R=20mm
True strain rate $[\frac{1}{s}]$
0.000
0.001
0.002
0.003
0.00
0.25
0.50
0.75
1.00
1.25
True strain [-]

(a)

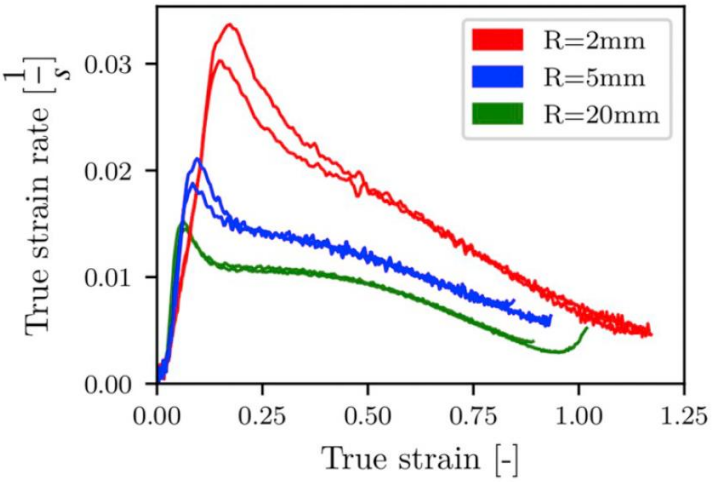
R=2mm
R=5mm
R=20mm
True strain rate $[\frac{1}{s}]$
0.00
0.01
0.02
0.03
0.00
0.25
0.50
0.75
1.00
1.25
True strain [-]

(b)

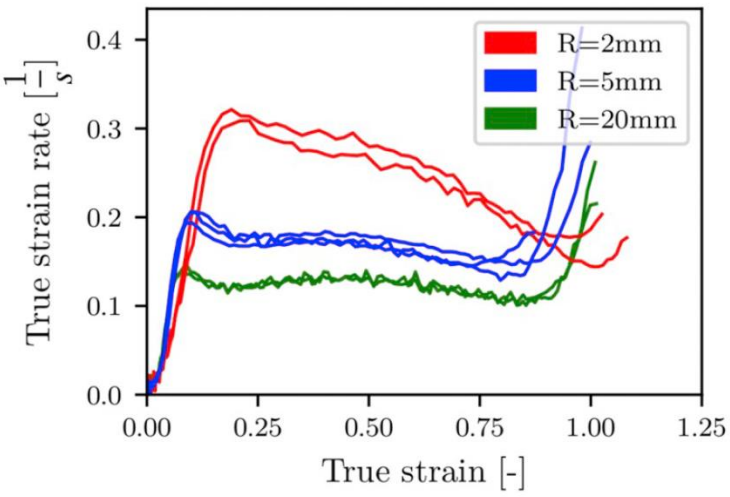

(c)

Figure 7 True strain rate vs. true strain curves for the notched specimens at nominal strain rate of (a) $10^{-4}\ s^{-1}$*, (b)* $10^{-3}\ s^{-1}$ *and (c)* $10^{-2}\ s^{-1}$.

Based on the pictures acquired by both cameras, the notch curvature was extracted from the contours and is shown in Figure 8. It is observed that the initial curvature at zero deformation agrees well with the reciprocal of the notch radius in the respective tests. Thereafter, a minor reduction of curvature, i.e., a slight straightening, occurs up to a true strain of approx. 0.05. This corresponds to the initial phase of the test before yielding. With further straining, the general impression is that the notch curvature increases with deformation until initiation of cold-drawing, which causes a subsequent reduction of the notch curvature. For a given notch radius, the evolution of curvature is rather similar at strain rates $10^{-4}\ s^{-1}$ and $10^{-3}\ s^{-1}$, while higher peak curvatures are observed for the highest strain rate for all notch radii.

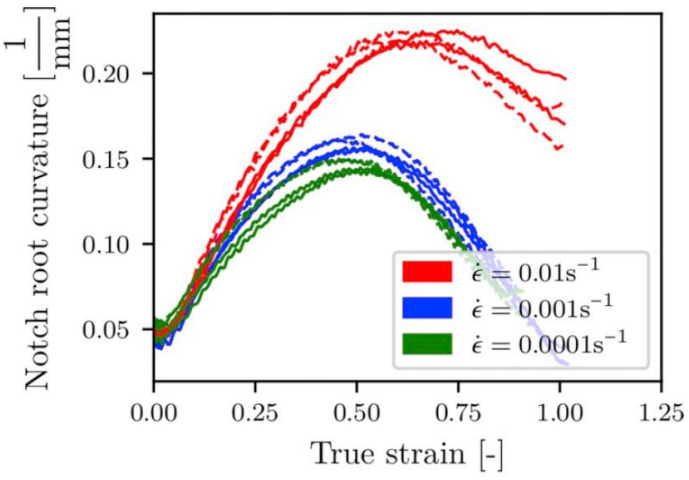

(a)

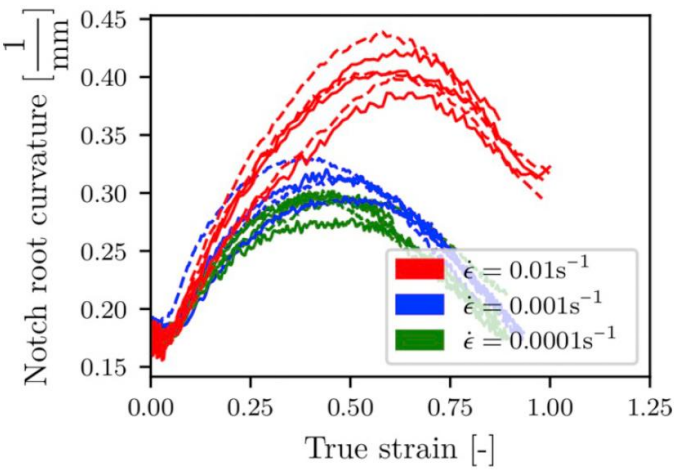

(b)

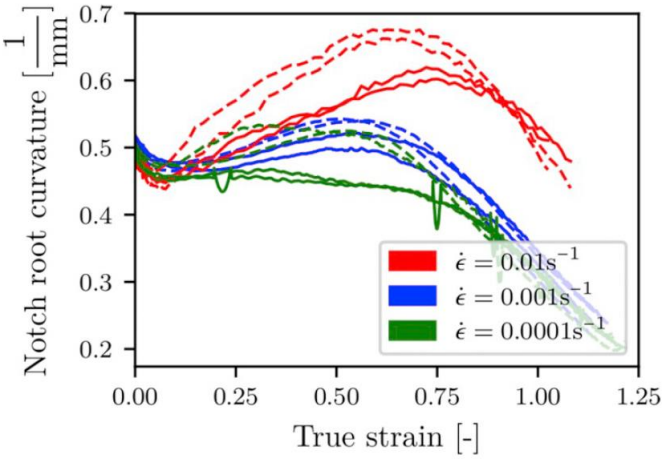

(c)

Figure 8 Notch curvature vs. true strain curves at three nominal strain rates for specimens with notch radius (a) 20 mm, (b) 5 mm and (c) 2 mm based on measurements from camera 1 (solid line) and camera 2 (dashed line).

Figure 9 shows the volume ratio λ_V, defined by Equation 4, as a function of the true strain. Clearly, there is substantial dilation, and λ_V increases monotonically up to the point of failure for all specimens. It is also observed that λ_V increases with decreasing notch radius, which implies increasing stress triaxiality in the notch region. The evolution of the volume ratio λ_V becomes less nonlinear with decreasing notch radii, and a nearly linear evolution is exhibited for the R2 specimens. All specimens deformed at a nominal strain rate of $10^{-2}\ \text{s}^{-1}$ exhibit a linearly increasing λ_V until failure.

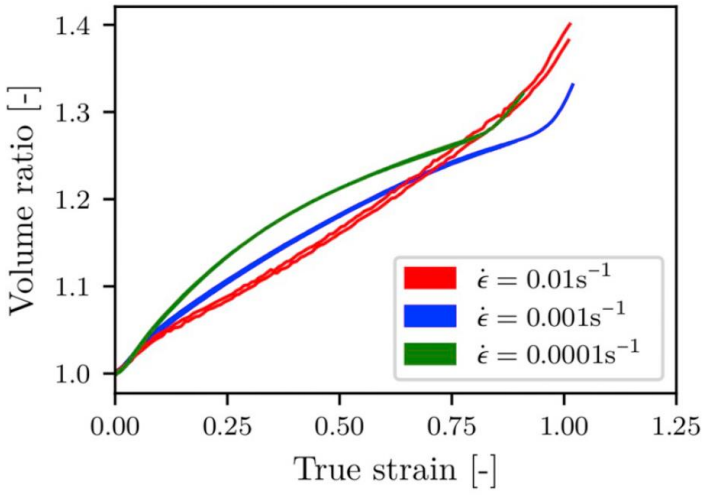
Volume ratio [-]
1.4
1.3
1.2
1.1
1.0
0.00
0.25
0.50
0.75
1.00
1.25
True strain [-]
$\dot{\epsilon} = 0.01\text{s}^{-1}$
$\dot{\epsilon} = 0.001\text{s}^{-1}$
$\dot{\epsilon} = 0.0001\text{s}^{-1}$

(a)

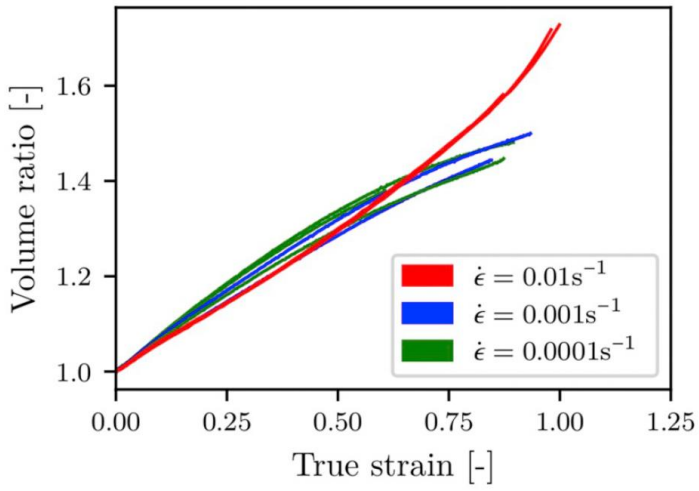
Volume ratio [-]
1.6
1.4
1.2
1.0
0.00
0.25
0.50
0.75
1.00
1.25
True strain [-]
$\dot{\epsilon} = 0.01\text{s}^{-1}$
$\dot{\epsilon} = 0.001\text{s}^{-1}$
$\dot{\epsilon} = 0.0001\text{s}^{-1}$

(b)

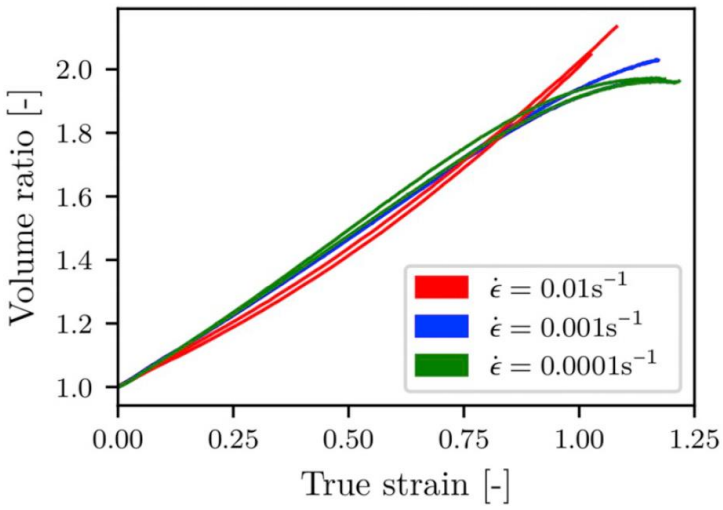

(c)

Figure 9 Volume ratio vs. true strain curves at three nominal strain rates for specimens with notch radius (a) 20 mm, (b) 5 mm and (c) 2 mm.

The evolution of the surface temperature with straining, as measured by infrared thermography, is shown in Figure 10. The surface temperature increases steadily with the deformation of the specimen and, at a given strain, it is higher for a higher nominal strain rate. At the highest strain rate, the peak surface temperature reaches about 46°C at the point of failure. On the other hand, the temperature increase is essentially negligible for the lowest strain rate, and it is around 5°C at the intermediate strain rate of 10^{-3} s^{-1}.

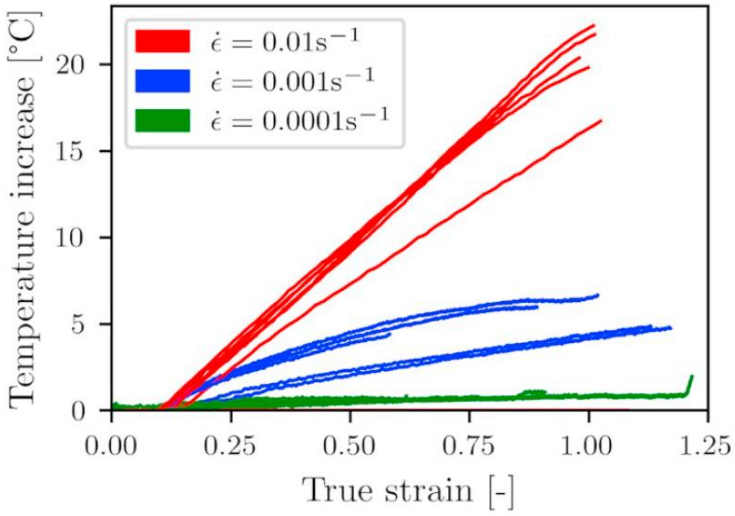

Figure 10 Evolution of surface temperature with true strain as measured by IR thermography in all tests.

4 Discussion

The surface deformation of all specimens was quantified by means of digital image correlation up to the stage where visible surface cracks were observed. As only in-plane displacement components are captured by the 2D DIC set-up, out-of-plane movements could produce spurious strains [23]. The ratio of spurious longitudinal strain to measured longitudinal strain is estimated for all deformations as

$$\xi = \frac{\Delta z}{z\varepsilon_l} \tag{5}$$

where Δz and z are the out-of-plane displacement of the surface and the object distance from the lens pinhole, respectively [23]. The peak value of ξ is estimated to 0.002 for the current set-up. Furthermore, Johnsen et al. [24] used the same cameras and optics, and demonstrated close agreement between the in-plane strains found from 2D and 3D DIC set-ups for a similar experimental configuration. Moreover, the radial strains obtained using DIC was compared with the strains calculated from the diameter evolution using contour tracking, also showing close coincidence. Thus, the out-of-plane displacement does not seem to disturb the strain measurements.

Owing to inaccuracies in the manufacturing process, small stepwise linear segments were observed along the notch of the specimens. These defects were particularly pronounced for the smallest notch radius. As the notch curvature is measured by fitting a circle to the notch contour employing an optimization algorithm, see Section 2.4, the deviation of the notch contour from a smooth arc imposes inaccuracies. As can be seen from Figure 8, the average notch curvature extracted from the two cameras deviates, indicating possible inaccuracies in the curvature extraction. Material anisotropy is another potential mechanism, which could cause variations in notch curvature along the circumference of the specimen but, as the notch root strains do not deviate significantly between cameras, this is considered a less likely mechanism.

The true stress vs. true strain curves, exhibiting pronounced softening after the point of initial yielding followed by hardening up to failure, are in agreement with the findings of Ognedal et al. [2]. Strain softening has been attributed to several physical mechanisms, such as ageing, void nucleation and void growth [11,15,16]. Ageing of a similar material has previously been investigated by Ognedal [21], where specimens were elongated to various states beyond the point of softening and stored for a range of durations. The stored specimens did not exhibit softening during subsequent loading, suggesting that ageing is not responsible for the softening of the material [21].

The true stress at initial yielding is observed to exhibit a log-linear dependence on the nominal strain rate, see Figure 6. Hence, the results conform to the Ree-Eyring model for isothermal conditions. In addition Figure 6 reveals that the yield stress does not depend much on the stress triaxiality ratio, which indicates a pressure-sensitive material behaviour. Factors such as the presence of voids in the material and void nucleation have been reported to cause pressure sensitive yield behaviour [25,26]. For a given strain rate, it is interesting to note that virtually identical yield stresses are found at the three triaxiality ratios imposed by the three notch radii. As has been

investigated by Ognedal et al. [16], the yielding of the material could be induced by void nucleation, which has been reported to be influenced by the stress triaxiality [25]. A coupling between yielding by void nucleation and stress triaxiality could, therefore, be a possible reason for the pressure dependence of this material.

After the onset of yielding, strain localization is observed in all specimens, indicated by an increase in strain rate and increasing notch curvature, see Figure 7 and Figure 8. The strain localization forms a visible neck within the notch for several specimens but, for the sake of clarity, the neck curvature is herein referred to as notch curvature. For further increasing strain, cold drawing is observed for the specimens deformed at strain rates of 10^{-4} s^{-1} and 10^{-3} s^{-1}. During cold drawing, the local strain rate and notch curvature decrease with straining. The specimens deformed at a nominal strain rate of 10^{-2} s^{-1} do not show a pronounced decrease in strain rate after yielding and a higher notch root curvature is reached before failure, indicating limited cold drawing. The absence of cold drawing for the highest strain rate could possibly be attributed to thermal softening, substantiated by the increased surface temperature during deformation, see Figure 10.

The nearly linear increase in volume ratio for R2 and R5 specimens resembles findings in several studies using the same technique to estimate the average volume ratio within the neck of the specimen [2,5,16]. The magnitude of the volume ratio demonstrates that significant pore fractions are present within the material. For the R20 specimens deformed at strain rates of 10^{-4} s^{-1} and 10^{-3} s^{-1}, the slope of the volume ratio vs. true strain curve decreases for increasing straining, indicating that a driving mechanism for void growth is influenced by the increasing strain. As stress triaxiality has been observed to be a governing parameter for void growth [7,11], the pronounced increase of notch curvature due to localization could be a possible explanation for the non-linear volume ratio evolution observed for the R20 specimens at strain rates of 10^{-4} $s^{-1}$and 10^{-3} s^{-1}. For the R20 specimens deformed at a nominal strain rate of 10^{-2} s^{-1}, the diameter contraction is larger for a given true strain, causing a lower estimated volume ratio. The volume ratio at failure is larger for all specimens deformed at a nominal strain rate of 10^{-2} s^{-1}, possibly due to the increased notch curvature. The R5 and R2 specimens exhibit a more linear volume ratio evolution with true strain, and the relative increase in notch curvature is smaller for these specimens.

5 Conclusions

An experimental study on a mineral-filled PVC material is presented in this article. Tension tests on axisymmetric notched samples with three different notch radii were performed at three different strain rates. The following main conclusions are drawn:

- The yield stress of the PVC material is pressure sensitive and essentially the same for the three notch radii at a given strain rate.
- A log-linear increase in the yield stress with increasing strain rate was found, in agreement with the Ree-Eyring model for isothermal conditions.
- Considerable volume changes were observed at the three investigated levels of stress triaxiality, all being relevant for engineering applications.

- A marked increase of temperature during plastic deformation was observed for the tests at the highest strain rate ($10^{-2}s^{-1}$), apparently affecting the true stress vs. true strain curves at large strains.

Acknowledgements

The authors gratefully appreciate the financial support from the Research Council of Norway through the Centre for Advanced Structural Analysis, Project No. 237885 (CASA). Mr. Trond Auestad is acknowledged for the invaluable help with the experimental set-up and performing the experiments.

Data availability statement

The raw/processed data required to reproduce these findings cannot be shared at this time due to technical or time limitations.

References

[1] N.J. Mills, The mechanism of brittle fracture in notched impact tests on polycarbonate, J. Mater. Sci. 11 (1976) 363–375. http://dx.doi.org/10.1007/BF00551448.

[2] A.S. Ognedal, A.H. Clausen, A. Dahlen, O.S. Hopperstad, Behavior of PVC and HDPE under highly triaxial stress states: An experimental and numerical study, Mech. Mater. 72 (2014) 94–108. http://dx.doi.org/10.1016/j.mechmat.2014.02.002.

[3] S. Guo, D. Torres, S. Weygand, C. Olagnon, R. Estevez, 3D study of the competitions between shear yielding and crazing for a variable thickness on ductile polymers, Eng. Fract. Mech. 33 (2015) 230–249. http://www.sciencedirect.com/science/article/pii/S001379441500497X.

[4] D.G. Legrand, Crazing, yielding, and fracture of polymers. I. Ductile brittle transition in polycarbonate, J. Appl. Polym. Sci. 13 (1969) 2129–2147. http://dx.doi.org/10.1002/app.1969.070131010.

[5] C. G'Sell, J.M. Hiver, A. Dahoun, Experimental characterization of deformation damage in solid polymers under tension, and its interrelation with necking, Int. J. Solids Struct. 39 (2002) 3857–3872. doi:10.1016/S0020-7683(02)00184-1.

[6] L. Laiarinandrasana, T.F. Morgeneyer, H. Proudhon, F. N'Guyen, E. Maire, Effect of multiaxial stress state on morphology and spatial distribution of voids in deformed semicrystalline polymer assessed by X-ray tomography, Macromolecules. 45 (2012) 4658–4668. doi:10.1021/ma3005247.

[7] G. Boisot, L. Laiarinandrasana, J. Besson, C. Fond, G. Hochstetter, Experimental investigations and modeling of volume change induced by void growth in polyamide 11, Int. J. Solids Struct. 48 (2011) 2642–2654. doi:10.1016/j.ijsolstr.2011.05.016.

[8] N. Brusselle-Dupend, E. Rosenberg, J. Adrien, Characterization of cavitation development while tensile testing PVF2 using 3D X-ray microtomography, Mater. Sci. Eng. A. 530 (2011) 36–50. doi:10.1016/j.msea.2011.09.009.

[9] L. Laiarinandrasana, T.F. Morgeneyer, H. Proudhon, C. Regrain, Damage of semicrystalline polyamide 6 assessed by 3D X-ray tomography: From microstructural evolution to constitutive modeling, J. Polym. Sci. Part B Polym. Phys. 48 (2010) 1516–1525. doi:10.1002/polb.22043.

[10] L. Laiarinandrasana, O. Klinkova, F. Nguyen, H. Proudhon, T.F. Morgeneyer, W. Ludwig, Three dimensional quantification of anisotropic void evolution in deformed semi-crystalline polyamide 6, Int. J. Plast. 83 (2016) 19–36. doi:10.1016/j.ijplas.2016.04.001.

[11] A.C. Steenbrink, E. Van Der Giessen, P.D. Wu, Void growth in glassy polymers, J. Mech. Phys. Solids. 45 (1997) 405–437. doi:10.1016/S0022-5096(96)00093-2.

[12] H.B. Chew, T.F. Guo, L. Cheng, Effects of pressure-sensitivity and plastic dilatancy on void growth and interaction, Int. J. Solids Struct. 43 (2006) 6380–6397. doi:10.1016/j.ijsolstr.2005.10.014.

[13] L. Cheng, T.F. Guo, Void interaction and coalescence in polymeric materials, Int. J. Solids Struct. 44 (2007) 1787–1808. doi:10.1016/j.ijsolstr.2006.08.007.

[14] S.Y. Fu, X.Q. Feng, B. Lauke, Y.W. Mai, Effects of particle size, particle/matrix interface adhesion and particle loading on mechanical properties of particulate-polymer composites, Compos. Part B Eng. 39 (2008) 933–961. doi:10.1016/j.compositesb.2008.01.002.

[15] H.E.H. Meijer, L.E. Govaert, Mechanical performance of polymer systems: The relation between structure and properties, Prog. Polym. Sci. 30 (2005) 915–938. doi:10.1016/j.progpolymsci.2005.06.009.

[16] A.S. Ognedal, A.H. Clausen, T. Berstad, T. Seelig, O.S. Hopperstad, Void nucleation and growth in mineral-filled PVC - An experimental and numerical study, Int. J. Solids Struct. 51 (2014) 1494–1506. http://dx.doi.org/10.1016/j.ijsolstr.2013.12.042.

[17] M. Andersen, An Experimental and Numerical Study of Thermoplastics at Large Deformations, 2016.

[18] N. Selles, F. Nguyen, T.F. Morgeneyer, H. Proudhon, W. Ludwig, L. Laiarinandrasana, Comparison of voiding mechanisms in semi-crystalline polyamide 6 during tensile and creep tests, Polym. Test. 49 (2016) 137–146. doi:10.1016/j.polymertesting.2015.11.019.

[19] P.A. Poulet, G. Hochstetter, A. King, H. Proudhon, S. Joannès, L. Laiarinandrasana, Observations by in-situ X-ray synchrotron computed tomography of the microstructural evolution of semi-crystalline Polyamide 11 during deformation, Polym. Test. 56 (2016) 245–260. doi:10.1016/j.polymertesting.2016.10.023.

[20] N. Selles, N. Saintier, L. Laiarinandrasana, Voiding mechanisms in semi-crystalline

polyamide 6 during creep tests assessed by damage based constitutive relationships and finite elements calculations, Int. J. Plast. 86 (2016) 112–127. doi:10.1016/j.ijplas.2016.08.004.

[21] A.S. Ognedal, Large-Deformation Behaviour of Thermoplastics at Various Stress States, NTNU, 2012.

[22] A. Savitzky, M.J.E. Golay, Smoothing and Differentiation of Data by Simplified Least Squares Procedures, Anal. Chem. 36 (1964) 1627–1639. doi:10.1021/ac60214a047.

[23] M.A. Sutton, J.-J. Orteu, H.W. Schreier, Image Correlation for Shape, Motion and Deformation Measurements, 2009. doi:10.1017/CBO9781107415324.004.

[24] J. Johnsen, F. Grytten, O.S. Hopperstad, A.H. Clausen, Experimental set-up for determination of the large-strain tensile behaviour of polymers at low temperatures, Polym. Test. 53 (2016) 305–313. doi:10.1016/j.polymertesting.2016.06.011.

[25] A. Needleman, A Continuum Model for Void Nucleation by Inclusion Debonding, J. Appl. Mech. 54 (1987) 525. doi:10.1115/1.3173064.

[26] A.C. Steenbrink, E. van der Giessen, On cavitation, post-cavitation and yield in amorphous polymer–rubber blends, J. Mech. Phys. Solids. 47 (1999) 843–876. http://www.sciencedirect.com/science/article/pii/S0022509698000751.